DOI 10.1007/s10652-016-9505-9

Flow and drag force around a free surface piercing cylinder for environmental applications

Thomas Ducrocq[1] · Ludovic Cassan[1] · Jacques Chorda[1] · Hélène Roux[1]

Abstract This paper investigates flows around a free surface piercing cylinder with Froude number $F > 0.5$ and Reynolds number around $Re = 50{,}000$. The aim of this work is to gain a better understanding of the flow behaviour in environmental systems such as fishways. The advances are based upon experimental and numerical results. Several flow discharges and slopes are tested to obtain both subcritical and supercritical flows. The drag force exerted on the cylinder is measured with the help of a torque gauge while the velocity field is obtained using particle velocimetry. For the numerical part, two URANS turbulence models are tested, the k-ω SST and the RNG k-ε models using the OpenFOAM software suite for subcritical cases, and then compared with the corresponding experimental results. With fishways applications in mind, the changes in drag coefficient C_d versus Froude number and water depth are studied and experimental correlations proposed. We conclude that the most suitable URANS turbulence model for reproducing this kind of flow is the k-ω SST model.

Keywords URANS · Piercing pier · Supercritical flow · Drag force · Environnemental applications

✉ Ludovic Cassan
lcassan@imft.fr

Thomas Ducrocq
thomas.ducrocq@imft.fr

Jacques Chorda
chorda@imft.fr

Hélène Roux
hroux@imft.fr

[1] Institut de Mécanique des Fluides, allee du Prof. Camille Soula, 31400 Toulouse, France

1 Introduction

Policies for the restoration or conservation of aquatic fields require a more accurate knowledge of physical phenomena. Indeed, a better insight into hydrodynamics will be useful for sediment transport and modelling of turbulent properties such as those encountered in complex environmental flows (energy dissipation, nutrient transport). Moreover, the hydrodynamic environment should be described spatially and temporally since the mean values on a stream cross-section are too low to enable the interactions between the hydraulics and the biology of the ecosystem to be properly described. Of particular interest is the understanding of the three dimensional flow structures in potential fish refuge areas (as encountered in the wakes of large obstacles or river bank zones). Similarly, with a properly modelled flow around obstacles, it should be possible to design hydraulic structures such as fishways in a more efficient manner [6, 9]. The 3D-modelling of a steep pass fishway [18] shows that, compared with experiment, the error may be significant. In a general sense, CFD validation for this kind of flow is still under investigation [4].

In this paper, we assess the ability of an Unsteady Reynolds Averaged Navier Stokes (URANS) numerical code to address ecohydraulic issues concerning emergent cylinders. In a recent paper, Kirkil and Constantinescu [15] performed Large Eddy Simulations (LES) around a circular pier and proved that this model can reproduce main flow structures as Horseshoe Vortices (HSV) and near wake structures. However, these simulations were conducted with a rigid top rather than a free surface and were therefore not suitable for representing high Froude number flows. In the article by Koo et al. [16], the influence of Froude number is studied but the configuration differs from the applications expected here as the waterdepth is much greater than the cylinder diameter, thus limiting the influence of the bed on the flow structures. The aim here is to assess the URANS modelling capability for flow having the two following characteristics: high Froude number and low waterdepth around a non-submerged cylinder. Although the URANS simulations are unable to reproduce the HSVs, they can provide pertinent information about the wake zone such as lateral oscillation or turbulent kinetic energy, which both have a significant impact on the fish resting zone. For a higher level of application, e.g. design of complete "nature-like" fishways [6], it is important that the drag forces on emergent cylinder arrays, including their variation as a function of Froude number, should be accurately computed. Moreover, these forces can contribute in improving roughness models for emergent vegetation, this being crucial for accurate computation of runoff flow over floodplains.

An experimental part aims to validate the simulations. A Particle Tracking Velocimeter (PTV) method was employed since laser velocimetry is difficult to implement due to significant free surface deformations and the occurrence of bubbles. Moreover, methods such as Acoustic Doppler Velocimetry (ADV) are too intrusive in relation to the water depths. A torque gauge is used to measure the drag force. These devices provide useful data for the design of fishways and validating the URANS simulations. The experiments are described in the following section; Sect. 3 presents the numerical model, the results are analysed in Sect. 4, and finally some examples for the implications for fish resting zones are provided.

2 Experiments

The experiments were carried out in a variable slope laboratory flume at the Institute of Fluid Mechanics of Toulouse (IMFT). The channel width B is 0.4 and 4 m in length (Fig. 1). The side walls and bottom are glass. A smooth PVC cylinder is set on the centreline of the channel 2 m from the upstream end. Its diameter D is 4 cm. An electromagnetic flowmeter provides the flow rate to an accuracy of 1%.

For the first series of experiments, the cylinder was connected to a torque gauge measuring the force in the longitudinal direction. The torque on the axis was provided by a piezoelectric probe at a frequency of 625 Hz. An initial averaged value (C_0) was measured for all channel slopes in the absence of flow. These measurements allowed the contribution of the obstacle weight to be taken into account (Fig. 2). In order to convert the torque signal into a force, the point of application of the force was assumed to be located at two-thirds of the waterdepth (≈3 cm from the bottom) corresponding to the hydrostatic pressure distribution. This assumption leads to an uncertainty less than 10% since the distance between the axis of the torque gauge and the bed is 43 cm (an error of 1 cm in the height of the point of application leads to a force of between 0.024 and 0.026 N).

The drag force F_{drag} is deduced from the total measured torque (C_m) taking account of the torque due to the weight C_0 and the lift force $F_{lift} = \rho g \frac{\pi D^2}{4}$:

$$F_{drag} = \frac{C_m - (C_0 - F_{lift} d)}{h_{axis} - 1/3 \times h} \tag{1}$$

where d is the distance between the axis and the centre of the cylinder, h_{axis} is the distance between the axis and the bottom and g is the gravitational constant (see Fig. 2).

The flow conditions are presented in the Tables 1 and 2. The discharges are 5, 10, 15, 20 and 25 L/s and several slopes were used to modify the Froude and Reynolds numbers (Re).

For some experiments a thin weir was added at the downstream end of the flume to increase the water depth and decrease the Froude number. The water depth was measured at three gauge points: at 10 cm upstream of the cylinder (h), at the upstream side of the cylinder (h_u) and at the downstream side of the cylinder (h_d).

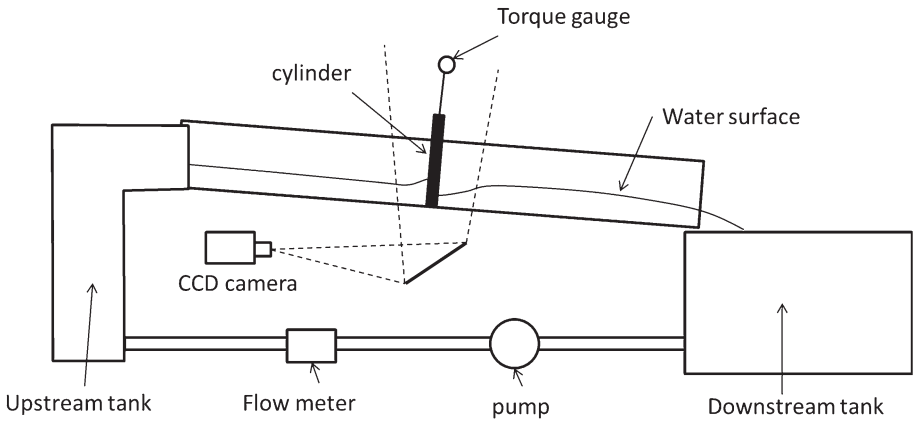

Fig. 1 Description of the experimental set-up

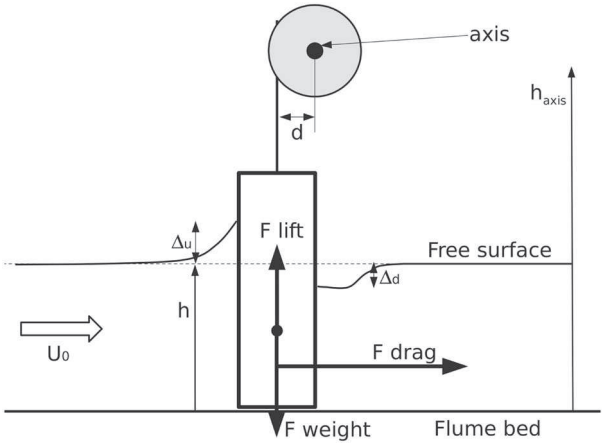

Fig. 2 Hydrodynamic force balance on the cylinder

Table 1 Flow conditions used for drag force measurements

Discharge (L/s)	Slope (%)	h_{weir} (m)	h (m)	h/D	U_0 (m/s)
5, 10, 15, 20, 25	0	0	(0.04–0.1)	(1–2.35)	(0.35–0.65)
5, 10, 15, 20, 25	0	0.05	(0.08–0.15)	(2–3.5)	(0.15–0.45)
10, 15, 20, 25	0	0.105	(0.15–0.2)	(4–5)	(0.15–0.3)
10, 15, 20	0.5	0	(0.05–0.07)	(1.35–1.85)	(0.45–0.7)
10, 15, 20	0.5	0.8	(0.03–0.045)	(0.7–1.15)	(0.85–1.1)
5, 10, 15, 20, 25	1	0	(0.02–0.06)	(0.5–1.3)	(0.7–1)
5, 10, 15, 20, 25	1	0.015	(0.02–0.06)	(0.5–1.5)	(0.7–1)
5, 10, 15, 20, 25	2	0	(0.035–0.04)	(0.85–1)	(1.1–1.4)
5,10, 15, 20, 25	2	0.015	(0.015–0.045)	(0.4–1.15)	(0.9–1.3)

Table 2 Froude et Reynlds numbers of flow used for drag force measurements

Discharge (L/s)	slope (%)	h_{weir} (m)	F	Re
5, 10, 15, 20, 25	0	0	(0.55–0.8)	(13,500–26,700)
5, 10, 15, 20, 25	0	0.05	(0.2–0.4)	(6.300–18,400)
10, 15, 20, 25	0	0.105	(0.1–0.2)	(6300–12,000)
10, 15, 20	0.5	0	(0.6–0.8)	(18,200–27,400)
10, 15, 20	0.5	0.8	(1.5–1.7)	(34,500–44,500)
5, 10, 15, 20, 25	1	0	(1.4–1.7)	(27,800–42,200)
5, 10, 15, 20, 25	1	0.015	(1.3–1.5)	(27,500–41,600)
5, 10, 15, 20, 25	2	0	(1.9–2.3)	(44,500–56,500)
5,10, 15, 20, 25	2	0.015	(1.9–2.3)	(37,000–52,000)

For velocity measurements, the cylinder was fixed to the channel to avoid vibration. A CCD (Charge Coupled Device) camera (2000×1200 pixels) captured the flow and allowed measurement of the velocity field. Two flow rates were used: 10 and 20 L/s and a

slope of 0%. The waterdepths h upstream of the cylinder are 0.06 and 0.08 m respectively, and the Froude numbers in this zone are 0.62 and 0.68 respectively. The image acquisition frequency is 250 Hz and a series of 2500 images was recorded for each discharge (Fig. 3). The water was seeded with plastic particles with a density close to 1, having diameters between 0.6 and 0.8 mm. They were illuminated with a LED lighting system attached to a side wall. An algorithm making use of the MATLAB imaging toolbox was developed to process these images, and is based on the following steps:

1. Each image is thresholded to detect the position of each particle.
2. They are converted into binary images, and the positions of the particles' centres and their sizes are stored.
3. Each particle is compared against all the particles from the previous image. Herein the detected particle is considered the same in both images if their sizes and light intensities are similar (to within a 10%) and the corresponding velocity is lower than some maximum value (usually 1.5 m/s).
4. Finally, the values of the velocity in both directions are assigned to the centre position (x, y).

After image processing, a statistical analysis was performed by combining the velocities in cells of 30×30 pixels, which corresponds to a physical cell of 5×5 mm. As a consequence, the size of the full image is 32×19 cm. The value of the velocities U and V in the longitudinal and transverse directions were computed by averaging all the measurements in the cell under consideration.

The sensitivity to each parameter (threshold, interval and size cell) was studied. The values given were deduced assuming statistical convergence at various locations. Obviously, this method provides depth-integrated data and is more relevant for 2D flows. However, it is used in this configuration because other techniques are difficult to realise. Indeed, the free surface deformations, bubbles and low water depths preclude PIV or ADV measurements. The experimental data were supplemented with a side view of the flow. For the side view, the same camera recorded 250 images with a frequency of 50 Hz. The averaged values of the images are plotted in Fig. 4. In the transverse direction, it is possible to locate the position of the free surface, particularly its upper position upstream of the cylinder and its lower position downstream of the cylinder.

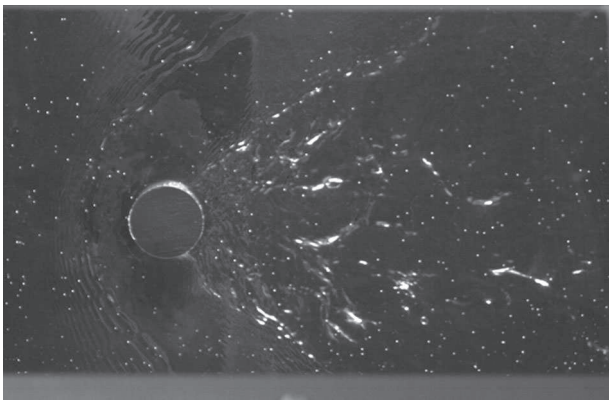

Fig. 3 Experimental image of PTV

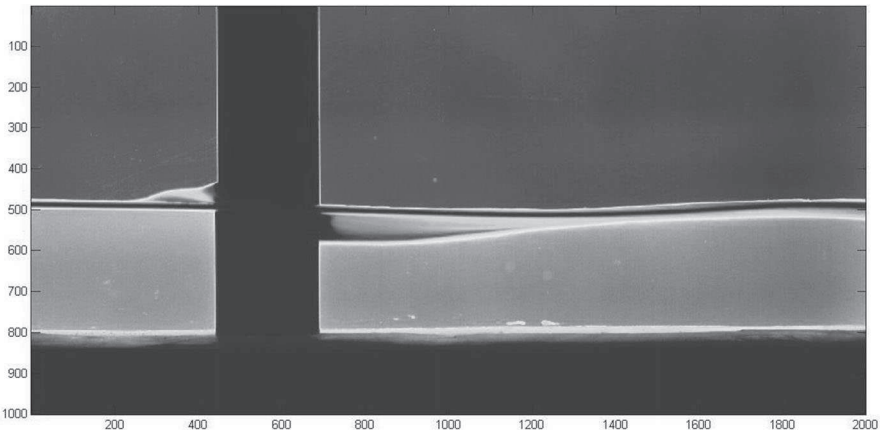

Fig. 4 Shadowgraph of the flow from the side (averaged image)

3 Flow modelling

OpenFOAM allows massively parallel computation and most of the classical turbulence models of fluid dynamics are implemented within it. The free surface position is fixed by the Volume Of Fluid (VOF) model [12, 13]. Two phases exist in the volume, namely water and air, and the volume fraction of each phase is calculated for each cell. Obviously, the sum of the air and water volume fractions in each cell is 1. The position of the free surface is assumed to be located at the centre of cells for which the water volume fraction is equal to 0.5.

A URANS method is chosen because it can be used in an environmental engineering case, unlike LES methods which are still highly CPU time consuming. Firstly, it is necessary to test several turbulence models in order to determine the one most appropriate for each application. Secondly, it is possible to estimate the incertainties created by these models. Although a RSM model seems relevant for this kind of separation flow [14, 23], two equations turbulence models are used as they are more widely used and accessible. The Re-Normalization Group (RNG) k-ε model is chosen because it provides good results for other free surface strained flow [5, 8, 23, 27]. In particular, it avoids overestimating the turbulent viscosity near stagnation points such as the front of the cylinder. This issue of the standard k-ε model is corrected by Baranya et al. [3] using the Kato-Launder modification. On the other hand, the k-ω SST (Shear Stress Transport) model is used as it is known to better reproduce the turbulence in the inner part of the boundary layer. Moreover, this model appears to behave well under separating flows and adverse pressure gradients.

The time step is variable to ensure the Courant number stays below 1 and the physical time simulated is 100 s. Observation of the flow showed it did not change significantly after 50 s of simulated time.

3.1 Geometry and mesh

The computational domain is identical to the experimental flume for code validation purposes. The dimensions and mesh details are described in Table 3. The mesh around the cylinder can be seen in Fig. 5.

3.2 Boundary conditions

A constant water discharge is set at the inlet boundary. For the air, the velocity is set to zero. A free fall is fixed at the outlet in order to reproduce the experimental condition. This implies a zero gradient for the velocity and zero pressure at this location. A no slip condition is set at the side walls and a wall function is used to model a smooth bed corresponding to the experimental set-up (glass). Finally, the boundary conditions at the top are set at atmospheric pressure and zero velocity gradient.

4 Results

4.1 Water depth

The position of the free surface provides the first validation of the numerical results. The experimental water surface profile is estimated using the sideviews. Figure 6 shows that both models correctly reproduce the surface profile at the centreline. The small difference between experimental and numerical waterdepths along the downstream side is due to the image processing. Indeed, the minimum depth on the image is not located on the centreline where the numerical dataset is extracted.

4.2 Velocity

An overall view of the measured velocity fields is presented in Fig. 7 for both experiments. The results are consistent with the literature data [2, 21]. A bow wave appears in front of the cylinder. As the Froude number is sufficiently high at the upstream end, the critical velocity can be reached at the minimum water depth (in the wake). Figure 7 shows that erroneous values can be found in the hydraulic jump because not all particles have been properly detected. In the near wake region, the flow structure appears more complex than those described by Roulund et al. [21] even if the length is also equal to the diameter D of the cylinder (Fig. 7). When the Froude number increases ($Q = 20$ L/s), the hydraulic jump moves downstream as indicated by the change in the transverse velocity direction.

A detailed description of the velocity fields is given in Fig. 8 where the velocity is normalized by the critical velocity $U_c = \sqrt{gh_c}$, with the critical depth h_c based on the total discharge. These are 0.63 and 0.78 m/s for $Q = 10$ L/s and $Q = 20$ L/s respectively. The velocities at the dashed lines in Fig. 7 are shown in Fig. 8. The simulation results are depth-averaged so as to be compared with experiment. At the upstream end, the experimental velocities are slightly underestimated in comparison with the bulk velocity. However, this discrepancy may come from the modification of the velocity field induced

Table 3 Flume characteristics

Width (m)	0.4
Length (m)	4
Slope	0%
Discharge (l/s)	10–20
Cells number	2,400,000
Cell size (L × l × h (m))	(0.0001–0.05) × (0.0001–0.02) × 0.001
$Y^+ = \frac{y \times u^*}{\nu}$	15–250

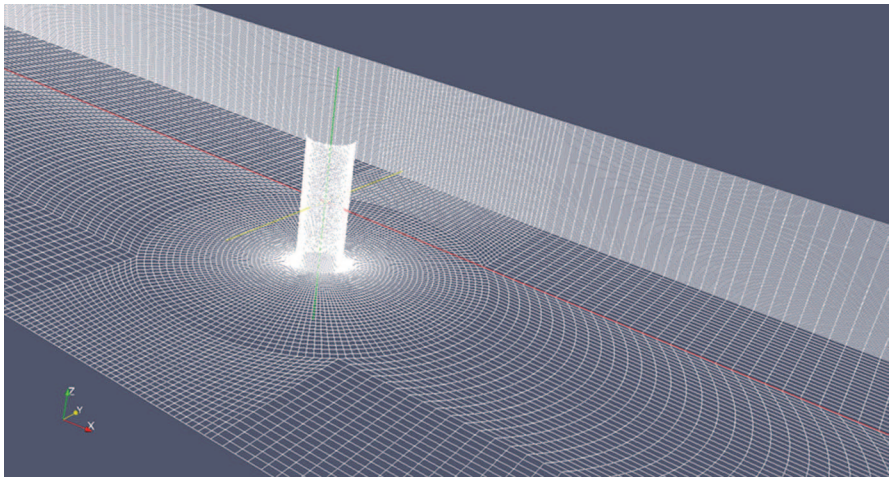

Fig. 5 Mesh around the cylinder

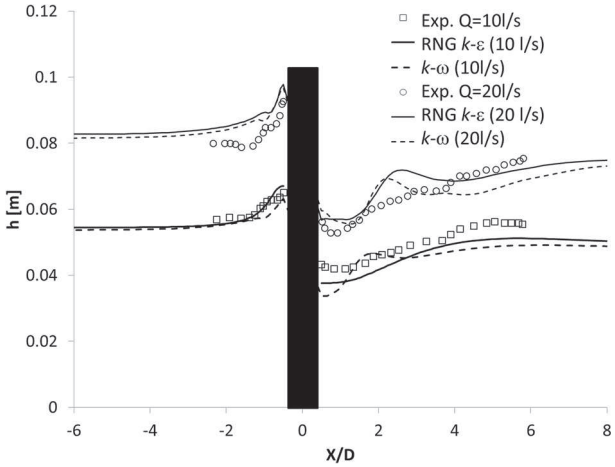

Fig. 6 Water depths at the centreline

by the cylinder. The presence of the cylinder in the experiments, as compared with the simulations, alters the speeds over a more extended zone upstream.

The difference between the two models is relatively small and only noticeable near the cylinder where the boundary layers are significant. But the k-ω SST model computes shorter recirculation zones for $y/D = 0$ and $y/D = 0.5$, in better agreement with the measurements. The transverse velocity confirms that the k-ω SST model provides a good calculation of the averaged velocity field. Unlike the RNG k-ε model, it involves a significant oscillation of the wake at the centreline. Therefore the k-ω SST model seems to be a more appropriate model for these flows around the cylinder.

Focussing on the recirculation zone behind the cylinder, the longitudinal and the lateral velocities U and V are shown in Fig. 9 at $x/D = 1$. The spanwise extension of the wake is well represented by the simulations. The experimental values of V in the wake are noisy,

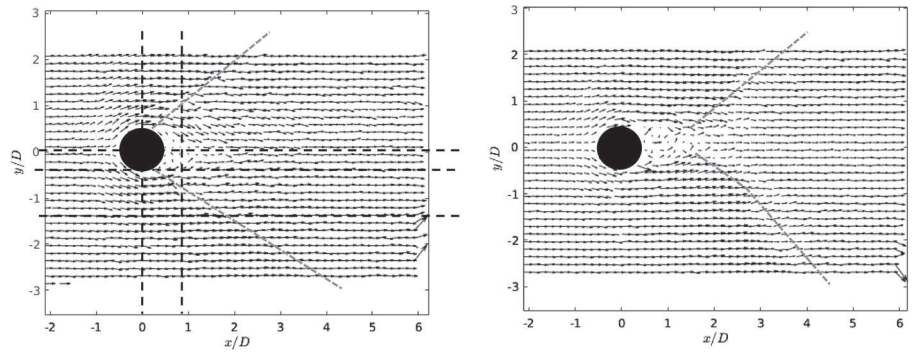

Fig. 7 Velocity field measured by PTV for $Q = 10$ L/s (*left*) and $Q = 20$ L/s (*right*). The *black dashed lines* represent the location of velocity profiles. The *grey dashed lines* show the hydraulic jump

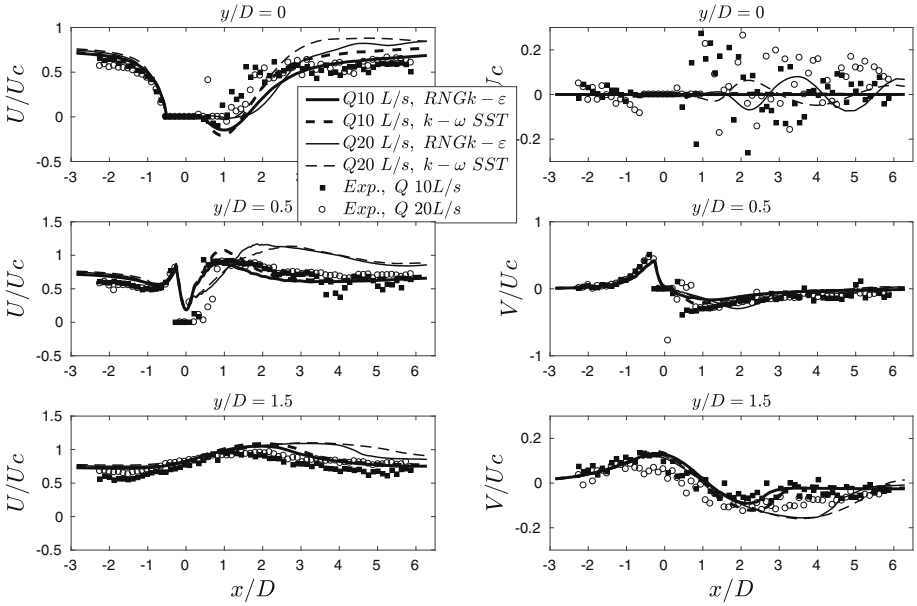

Fig. 8 Longitudinal velocity profiles in the X direction for various spanwise positions

but this noise can be explained by the vertical averaging process as the vertical flow is highly non uniform in this area.

In summary, the consistency between experiment and model shows that the URANS approach is suitable for computing depth-averaged velocities Tran et al. [25]. It might then be worthwhile to use CFD modelling to provide useful information for fish applications.

4.3 Drag force

As previously explained, the first experiments were carried out to obtain a better understanding of the hydraulic resistance of a cylinder in supercritical flows. Both can then be used to help with the design of fishways and validate the URANS simulations. The drag

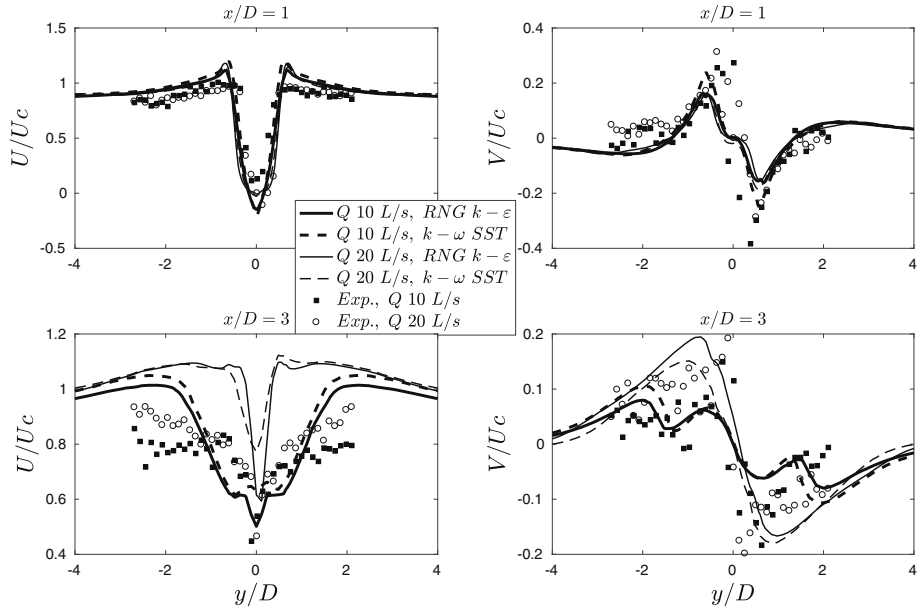

Fig. 9 Transverse velocity profiles in the y direction for various streamwise positions

force is extracted from simulations by integrating the pressure and viscous shear stresses on the obstacle at each time step. The experimental and numerical drag coefficients are computed from the drag force using Eq. (2) and are shown in Fig. 10:

$$C_d = \frac{2F_{drag}}{\rho h D U_0^2} \tag{2}$$

Figure 10 shows that the drag coefficient is not constant with Froude number. As a consequence, the methodology applied by Cassan et al. [6] is used to explain the variation in C_d and is based on the following assumption: the velocity field around the cylinder is responsible for the drag force modification, even if the drag coefficient remains constant.

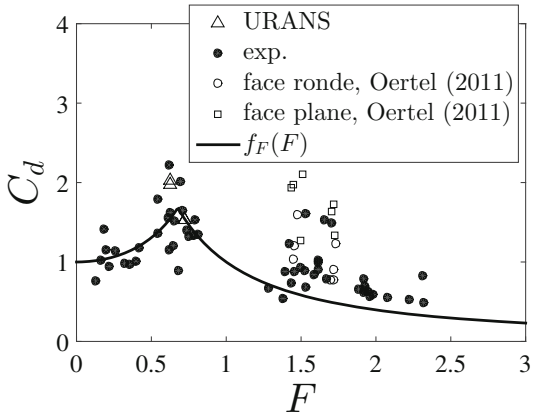

Fig. 10 Variation of drag coefficient as a function of Froude number

The influence of the Froude number depends on the vertical contraction of the water depth (in subcritical flow) and the regime transition (in supercritical flow) leading to an acceleration of the flow.

To quantify the change in drag coefficient for subcritical flows, it is necessary to take into account the free surface deformation around the cylinder. The experimental results are plotted in Fig. 11 in dimensionless form. The run-up height is quantified by $\Delta_u = (h_{max} - h)/h$ and changes in accordance with Bernoulli's theorem ($0.5\ F^2$). The depression height, defined by $\Delta_d = (h - h_{min})/h$, is plotted according to Chaplin and Teigen [7] who found the expression $\frac{h}{D} \times \Delta_d = 0.286F^2$ for the depression variation. Although Chaplin and Teigen [7] used a greater water depth with a larger range of Froude numbers, the results have the same tendancy. The difference can be explained by the interaction with the bed because the pier does not touch it in Chaplin and Teigen [7].

For calculating the drag coefficient, Qi et al. [19] studied the effect of the flow contraction due to the ratio of a prism width over the flume width. In the paper, they recall the empirical formula used by Raju et al. [20]: $C_d = C_{d0}(1 - D/B)^{-1.35}$. However, this is not sufficient to fully explain the modifications of the drag coefficient in this study. Therefore, another correction is proposed and described below. Cassan et al. [6] considered an appropriate reference velocity for the drag force: U_{drag}.

$$F_{drag} = \frac{1}{2}\rho C_d U_{drag}^2 Dh \tag{3}$$

$$= \frac{1}{2}\rho C_{d0} f_{h_*}(h_*) f_F(F) U_0^2 Dh \tag{4}$$

where $h_* = h/D$; the function $f_F(F) = \left(U_{drag}/U_0\right)^2$ allows the Froude number to be taken into account and $f_{h*}(h_*) = C_d/C_{d0}$ is an experimental correlation representing the influence of the bed.

The continuity equation integrated in the transverse direction provides an estimate of the ratio of the bulk velocity to the velocity due to the free surface contraction:

$$\frac{U_{drag}}{U_0} = \frac{h}{h_{min}} = \frac{1}{1 - 0.5F^2} \tag{5}$$

When transition occurs, the velocity around the cylinder is approximated by the critical velocity. This becomes:

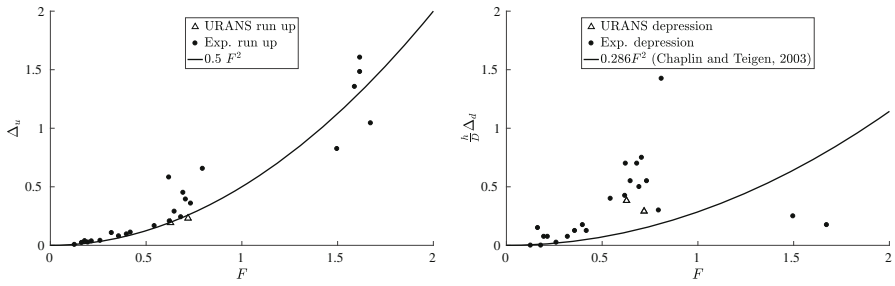

Fig. 11 Deformation of the free surface at the centreline (run-up on the *left* and depression on the *right*)

$$\frac{U_{drag}}{U_0} = F^{-2/3} \tag{6}$$

Combining Eqs. (5) and (6), the final $f_F(F)$ is given by:

$$f_F(F) = min\left(\frac{1}{1-0.5F^2}, F^{-2/3}\right)^2 \tag{7}$$

In Fig. 10, the drag coefficients from Eq. (2) are plotted along with the experimental results from Oertel et al. [17]. Although the experimental data confirm that Eq. (7) (and associated assumptions) can explain the general trend of C_d, another phenomenon may influence it. The same results led Cassan et al. [6] to propose the following experimental correlation for $f_{h*}(h_*)$:

$$f_{h_*}(h_*) = 1 + \frac{0.4}{h_*^2} \tag{8}$$

Figure 12 demonstrates that the C_d corrected by $f_F(F)$ can also be calculated by the correlation established for nature-like fishways. Similarly, the correction of C_d with Eq. (8) provides new experimental values of C_d as a function of F (Fig. 13). The experimental values are now consistent with the proposed formulation of $f_F(F)$ (Eq. 7) for all hydraulic conditions (see Fig. 13). The data from Oertel et al. [17] are also in good agreement with Eq. (7) though the C_d values are greater, since for plane faces the values of C_{d0} are greater than for a cylinder. Moreover, we assumed C_{d0} does not change with the Reynolds number. By analogy with 2D flows, this assumption can be true only within a limited range of Reynolds numbers. As a consequence, further studies are necessary to explore the influence of the Reynolds number on drag force with a strong influence due to the bed. For instance, the bed's boundary layer thickness is not taken into account since the walls are smooth, but it can be significant in real flows. Regarding C_d, the numerical results are in agreement with the experimental ones; this result also supports the suitability of the URANS method in reproducing these kinds of environmental flows.

4.4 Implication for fish resting zone

In order to study the implication for fish, the flows using the URANS models are analysed with the previous validation of the CFD results in mind. These simulations indicate a flow pattern similar to that given in Kirkil and Constantinescu [15]. Moreover, the computed

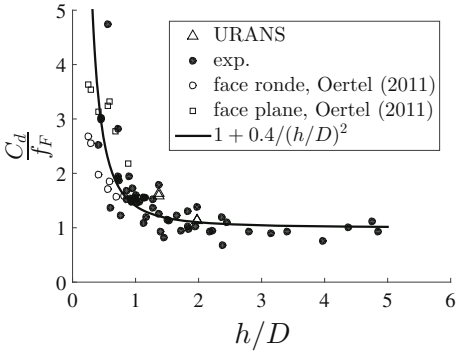

Fig. 12 Drag coefficient corrected by $f_F(F)$

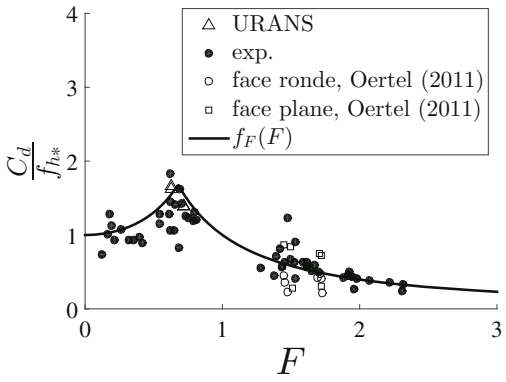

Fig. 13 Drag coefficient corrected by $f_{h_*}(h_*)$

streamlines (Fig. 14) are in good agreement with a qualitative observation of the particles in the flow. In particular, at the downstream side of the cylinder, vertical velocities are upward and two oscillating recirculation zones are detected at the surface in the wake area. The model results are also consistent with the vortices found for confined flows ($h/D \approx 1$) and low Froude numbers [2]. At the centreline, a large recirculating flow with a horizontal axis is observed between the obstacle and $X/D = 2$.

The two turbulence models induced a similar flow pattern, detailed in Fig. 15 along the longitudinal centre plane. The length of the resting zone can be taken as less than two diameters whatever the Froude number. However, the Froude number ($F > 0.5$) involves significant vertical velocities by comparison with low F flows [11]. The magnitude of the velocities is almost 25% of the longitudinal velocity, which can be significant if the wake is used as a fish resting zone.

Similarly, the URANS model provides the distribution of the turbulent kinetic energy k. For instance, Fig. 16 shows that the wake is mainly turbulent near the surface. Indeed, fish are particularly sensitive to these physical parameters [24]. Recall that the HSVs are not reproduced near the bed by the URANS simulation.

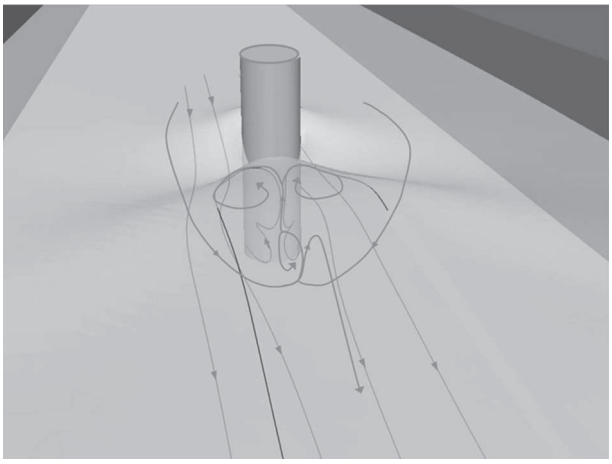

Fig. 14 Flow pattern and free surface for the simulation with $Q = 10$ L/s

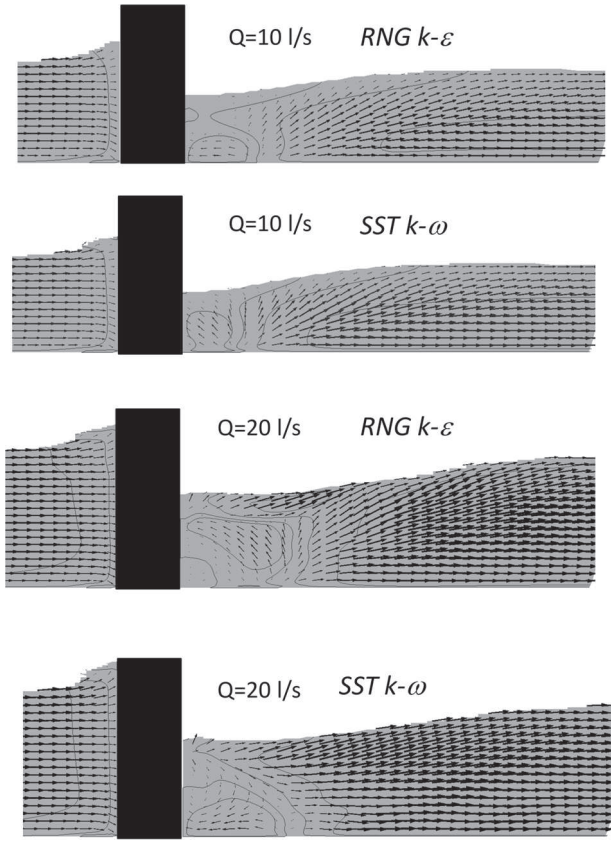

Fig. 15 Velocity field in the centre plane for the two URANS models, using two different discharges at $t = 100$ s

For $Q = 20$ L/s, the downward velocity behind the obstacle is due to the lateral oscillations of the wake (Figs. 8, 16). This phenomenon is observed mainly in the zone near the bed with the SST $k - \omega$ model. For $Q = 10$ L/s the wake is almost steady, which might be explained by the low waterdepth and therefore by the influence of the bed. For the same Reynolds number, Ferrand et al. [10] showed that URANS simulations are able to reproduce the von Karman vortex street. to find out whether the oscillation can be related to this phenomenon, the lateral velocity at the centreline and $X/D = 2$ is treated with a Welch's method plus Hanning window. The results between 80 and 100 s of simulation time are used. The Strouhal number is defined as:

$$St = \frac{fD}{U_0} \tag{9}$$

where f is the frequency.

The spectra obtained in the wake (Fig. 17) confirm that the oscillations are greater near the bed since the power spectra decrease with the distance to the bed. They also indicate that the Strouhal number (Fig. 17) is overestimated as compared with the experimental value of 0.2 [1]. The same observation is made by Ferrand et al. [10] with similar URANS

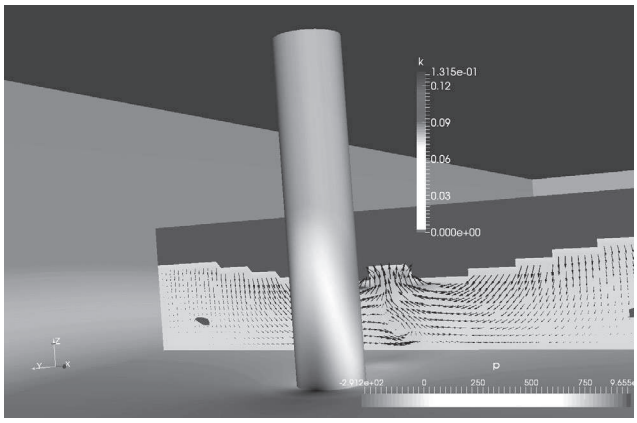

Fig. 16 Transverse and vertical velocity at the plane $X/D = 2$. The density of grey in the plane varies according to k and the wall according to pressure

simulations. Yu et al. [26] found a better value for Strouhal number ($S_t = 0.23$) but performed LES simulations which are much more accurate in the calculation of the turbulent field. However, in a similar way to this study, the oscillation magnitudes decrease with the distance to the bed. However, if the considered velocity at the downstream obstacle is greater than U_0, then the Strouhal number decreases. Indeed, the velocity represents the vortex advection. However, in accordance with the experimental and numerical results (Fig. 8), the velocity around the cylinder is modified by the free surface deformation.

Here, results directly applicable to fish resting zones are not given since the Froude similarity may be insufficient for this kind of flow to be properly computed (turbulent properties or boundary layers problem, as mentioned above). Nevertheless, the URANS simulation proved to be useful in providing the hydrodynamic parameters that influence fishes behaviour. Among both tested turbulent models, the SST k-ω model appears to be the most suitable for reproducing wake flows.

Fig. 17 Spectra of transverse velocity fluctuation at *X*/*D*

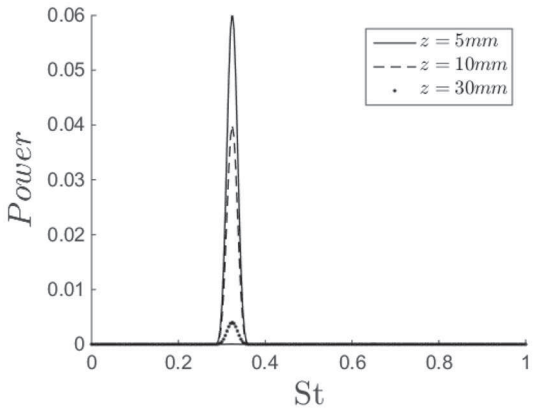

5 Conclusion

Simulations of the flow around a cylinder are performed with relatively high Froude number ($F > 0.5$) corresponding to environmental flows such as resting zones during hydropeaking or in fishways. To estimate the effect of gravity, the deformation of the free surface is computed with a VOF model and two turbulence models are tested. The numerical results are compared with experimental velocity fields integrated over depth and drag forces exerted on the cylinder. The C_d values from URANS simulations are consistent with measurements even if they are higher than common values. The explanation for the overestimated coefficients can be inferred from the experiments and the role of the bulk velocity around the cylinder is also put forward for the calculation of the drag force. It is then shown that the SST k-ω model is suitable for the purposes of the study and efficiently represents the velocities near the cylinder, something that is hard to demonstrate experimentally. Although less accurate than LES, the URANS simulations allow the oscillating velocities observed in the wake as well as the turbulent kinetic energy to be estimated. These hydrodynamic parameters are crucial in ensuring that this wake area is a resting zone for fish.

The perspectives are the computation of supercritical flows to test if the VOF and SST k-ω models are relevant to reproduce phenomena for environmental applications. A better understanding of the flow around submerged obstacles will complete the study because the water flowing over the top of the obstacle can lead to significant decreases in the amplitudes of oscillations [22] and drag forces.

References

1. Ahlborn B, Seto ML, Noack BR (2002) On drag, Strouhal number vortex-street structure. Fluid Dyn Res 30(6):379–399
2. Akilli H, Rockwell D (2002) Vortex formation from a cylinder in shallow water. Phys Fluids 14(9):2957–2967
3. Baranya S, Jôzsa J, Napoli E (2010) Field and numerical study of river confluence flow structures. In: Fifth international conference on fluvial hydraulics, River Flow 2010
4. Bousmar D, Li Z, Baugnee A, Degreff, J.-C (2015) Flow pattern in fish passes: comparison of numerical models. In: E-proceedings of 36th IAHR world congress
5. Cassan L, Belaud G (2012) Experimental and numerical investigation of flow under sluice gates. J Hydraul Eng 138:367–373
6. Cassan L, Tran TD, Courret D, Laurens P, Dartus D (2014) Hydraulic resistance of emergent macroroughness at large Froude numbers: design of nature-like fishpasses. J Hydraul Eng 140(1–9):04014043
7. Chaplin JR, Teigen P (2003) Steady flow past a vertical surface-piercing circular cylinder. J Fluids Struct 18:271–285
8. Dargahi B (2006) Experimental study and 3d numerical simulations for a free-overflow spillway. J Hydraul Eng 132(9):899–907
9. Duguay J, Lacey J (2014) Numerical validation of an innovative fish baffle. Design in response to fish passage issues at perched culverts. In: CSPI Technical Bulletin
10. Ferrand P, Boudet J, Caro J, Aubert S, Rambeau C (2006) Analyses of URANS and LES capabilities to predict vortex shedding for rods and turbines. In: Hall K, Kielb R, Thomas J (eds) Unsteady aerodynamics, aeroacoustics and aeroelasticity of turbomachines. Springer, Dordrecht, pp 381–393
11. Graf WH, Yulistiyanto B (1998) Experiments on flow around a cylinder; the velocity and vorticity fields. J Hydraul Res 36(4):637–654
12. Guler I, Behr M, Tezduyar T (1999) Parallel finite element computation of free-surface flows. Comput Mech 23:117–123
13. Hirt C, Nichols B (1981) Volume of fluid (VOF) method for the dynamics of free boundaries. J Comput Phys 39(1):201–255

14. Jau-Yau L, Jian-Hao H, Chuan-Yi W, Kun-Zheng L, Han-Chung Y (2003) Measurement and simulation of turbulent flow in a steep open-channel with smooth boundary. J Chin Inst Eng 26:201–210
15. Kirkil G, Constantinescu G (2015) Effects of cylinder Reynolds number on the turbulent horseshoe vortex system and near wake of a surface-mounted circular cylinder. Phys Fluids 27(7)
16. Koo B, Yang J, Mo MYS, Stern F (2014) Reynolds and Froude number effect on the flow past an interface-piercing circular cylinder. Int J Nav Archit Ocean Eng 6(3):523
17. Oertel M, Peterseim S, Schlenkhoff A (2011) Drag coefficients of boulders on a block ramp due to interaction processes. J Hydraul Res 49:372–377
18. Plymesser K (2014) Modeling fish passage and energy expenditure for American shad in a steppass fishway using a computation fluid dynamics model. Ph.D. thesis, Montana State University, Dept. of Civil Engineering, USA
19. Qi ZX, Eames I, Johnson ER (2014) Force acting on a square cylinder fixed in a free-surface channel flow. J Fluid Mech 756:716–727
20. Raju KGR, Rana OPS, Asawa GL, Pillai ASN (1983) Rational assessment of blockageeffect in channel flow past smooth circular cylinders. J Hydraul Res 21:289–302
21. Roulund A, Sumer B, Fredsoe J, Michelsen J (2005) Numerical and experimental investigation of flow and scour around a circular pile. J Fluid Mech 534:351–401
22. Sadeque M, Rajaratnam N, Loewen M (2009) Effects of bed roughness on flow around bed-mounted cylinders in open channels. J Eng Mech 135(2):100–110
23. Salaheldin TM, Jasim I, Hanif Chaudhry M (2004) Numerical modeling of three-dimensional flow field around circular piers. J Hydraul Eng 130:91–100
24. Santos JM, Silva A, Katopodis C, Pinheiro P, Pinheiro A, Bochechas J, Ferreira MT (2012) Ecohydraulics of pool-type fishways: getting past the barriers. Ecohydraulic approaches for restoring habitat connectivity and suitability. Ecol Eng 48:38–50
25. Tran DT, Chorda J, Laurens P, Cassan L (2016) Modelling nature-like fishway flow around unsubmerged obstacles using a 2D shallow water model. Environ Fluid Mech 16(2):413–428
26. Yu G, Avital EJ, Williams JJR (2008) Large eddy simulation of flow past free surface piercing circular cylinder. J Fluids Eng 130(1–9):101304
27. The OpenFOAM Foundation. www.openfoam.org.